ACS OMEGA

http://pubs.acs.org/journal/acsodf

Article

Rapid Characterization of Solid Tumors Using Resonant Sensors

Andee M. Beierle,[▽] Colin H. Quinn,[▽] Hooper R. Markert, Adam Carr, Raoud Marayati, Laura V. Bownes, Sara Claire Hutchins, Jerry E. Stewart, Benjamin Hill, Michael Ohlmeyer, Nigel F. Reuel,* and Elizabeth A. Beierle*

Cite This: *ACS Omega* 2022, 7, 32690−32700

Read Online

ACCESS | Metrics & More | Article Recommendations | Supporting Information

ABSTRACT: Cancer continues to be a significant cause of non-traumatic pediatric mortality. Diagnosis of pediatric solid tumors is paramount to prescribing the correct treatment regimen. Recent efforts have focused on non-invasive methods to obtain tumor tissues, but one of the challenges encountered is the ability to obtain an adequate amount of viable tissue. In this study, a wireless, inductor-capacitor (LC) sensor was employed to detect relative permittivity of pediatric tumor tissues. There is a comparison of resonant frequencies of tumor tissues between live versus dead tissues, the primary tumor tissue versus tissue from the organs of origin or metastasis, and treated versus untreated tumors. The results show significant shifts in resonant frequencies between the comparison groups. Dead tissues demonstrated a significant shift in resonant frequencies compared to alive tissues. There were significant differences between the resonant frequencies of normal tissues versus tumor tissues. Resonant frequencies were also significantly different between primary tumors compared to their respective metastases. These data indicate that there are potential clinical applications of LC technology in the detection and diagnosis of pediatric solid tumors.

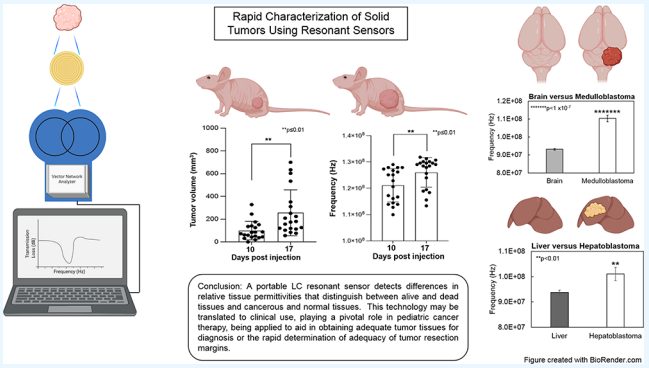

INTRODUCTION

Cancer continues to be a significant cause of non-traumatic childhood mortality. For pediatric solid tumors, rapid and accurate diagnosis is critical to prescribing the correct treatment regimen as treatments vary widely not only between tumor types but also between different biologic variables characterizing the tumors associated with staging. Current paradigms for the diagnosis of these cancers frequently involve tumor biopsy and investigation of the specimens with histology, immunohistochemistry, and genetic characterization. The ability to provide the pathologist with an adequate quantity of viable tissue is essential to the successful completion of the studies necessary for diagnosis and treatment planning. Historically, methods to obtain tumor tissue specimens involved an invasive procedure under general anesthesia often requiring a postoperative hospital admission.[1] Investigators have been focusing efforts to shift to less invasive biopsy methods, especially for children, to reduce exposure to general anesthetics, decrease blood loss, and avoid hospital admission.[2] These less invasive techniques, however, require immediate analysis of viability of the tumor biopsy specimens to prevent the need for a repeat biopsy. Depending on the environment, these examinations may require lengthy evaluations including transporting specimens from the operating theater to the pathology suite followed by frozen section processing and examination. We propose that a method capable of providing evaluation of the quality of tumor specimens in real-time in the operating room would be useful.

An inductor-capacitor (LC) resonator is a simple circuit that has an inherent resonant frequency at which inductively coupled power is most efficiently transferred.[3] It may be rendered into a sensor by engineering circuit elements such that alterations in temperature, pressure, humidity, or biologic analytes will change the inductance and/or capacitance of the circuit resulting in changes in the resonant frequency of the system.[3] Shifts in resonant frequencies are then detected contact-free by antennas connected to a vector network analyzer (VNA). The concept of studying resonant frequency in biologic systems is not a new one. Investigators have utilized LC sensors to detect changes in dielectric properties in several biologic systems including monitoring wound healing,[4] gastric pressure,[5] and intracranial pressure[6] and detecting the presence of urine[7] or sweat.[8] Other investigators have studied the changes in relative permittivites as applied to adult cancer

Received: July 9, 2022
Accepted: August 23, 2022
Published: September 2, 2022

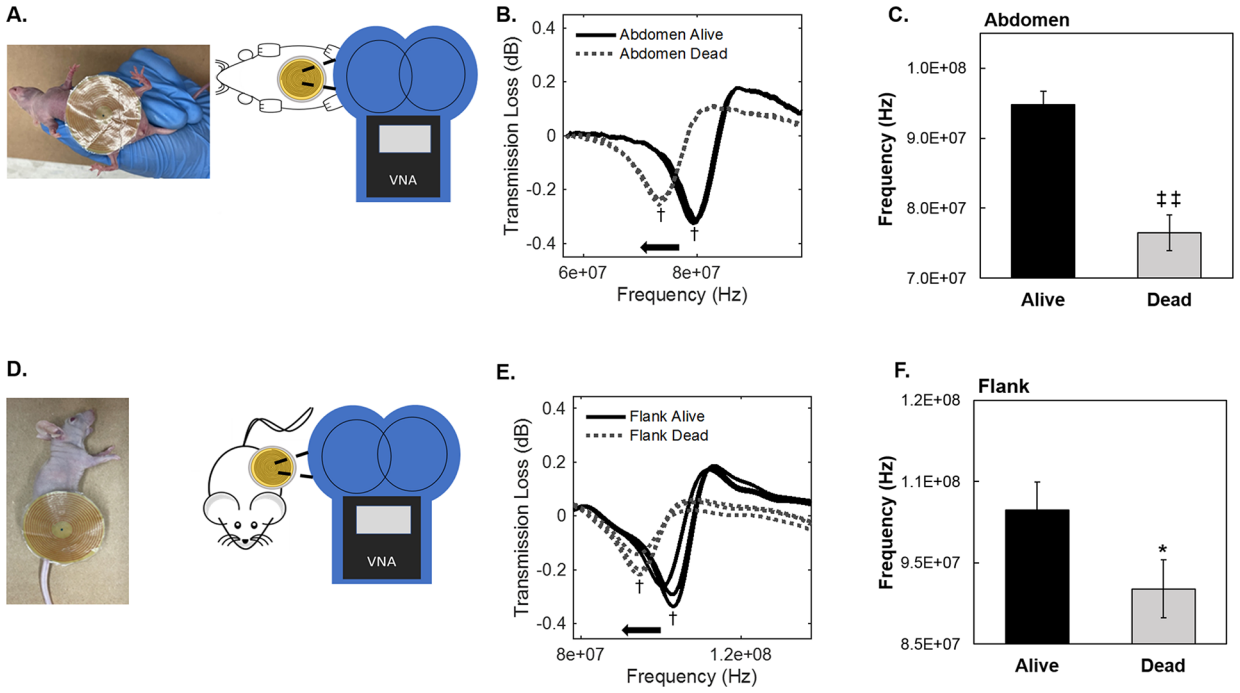

Figure 1. Scanning murine tissue using the LC sensor. (A) To scan the mouse abdomen, the resonant sensor was placed directly onto the abdomen of the animal and the VNA was positioned 1 cm above the sensor. Scans were obtained prior to (alive) and 5 min following (dead) euthanasia (n = 16). (B) Representative graph of the output by the MetroVNA of the scans from one animal demonstrating the decrease in resonant frequency (measured at trough, dagger symbol) of the abdominal tissue by a left shift (arrow) on the x axis of the dead abdominal tissue peaks in comparison to the alive abdominal tissue peaks. (C) Compiled data from 16 animals revealed that the resonant frequency values of abdominal tissue significantly decreased after the animals were euthanized. (D) Flank scans were obtained by placing the resonant sensor onto the flank of the animal and positioning the VNA 1 cm above the sensor. Scans were obtained prior to (alive) and 5 min following (dead) euthanasia (n = 8). (E) Representative scans from one animal. There was a left shift on the x axis of the dead flank tissue peaks compared to the alive flank peaks (arrow). (F) There was a statistically significant decrease in resonant frequency values of the mouse flank following euthanasia. A minimum of three scans were obtained for each data point. Photos obtained by the authors. Data reported as mean ± standard error of the mean (SEM). Student's t-test was used to determine statistical significance. $^{*}p \leq 0.05$, $^{‡‡}p \leq 1 \times 10^{-7}$.

types, and investigators have reported a variation in relative permittivity between normal and cancer specimens, including liver and breast cancer.[9,10] The notion of utilizing changes in relative permittivites in pediatric solid tumors is unique and to our knowledge has not yet been reported.

To monitor changes in tissue permittivity in the current study, we designed a passive, Archimedean spiral resonant sensor copper patch that was embedded into a commercial wound dressing that transduced the system resonant frequencies to an external reader antenna connected to a VNA. We hypothesized that this passive LC sensor system could characterize pediatric solid tumors based upon differences in the relative permittivity of the tissues. We evaluated common pediatric solid tumors including neuroblastoma, hepatoblastoma, neuroendocrine, osteosarcoma, and medulloblastoma human tumors propagated in murine models.

RESULTS

Scanning Murine Tissue Using the LC Sensor. To determine the ability of the LC resonant sensor to detect changes in relative permittivity of the murine tissues, we used a configuration that has been previously described.[3] For the current experiments, the resonant sensor was placed on the abdomen of the animal and VNA was positioned 1 cm above the sensor (Figure 1A). We obtained a minimum of three scans prior to euthanasia (live tissue) and 5 min post-euthanasia (dead tissue) for each animal. A representative output by the MetroVNA of the scans from one animal demonstrates the decrease in resonant frequency of the abdominal tissue by a left shift on the x axis of the dead abdominal tissue peaks in comparison to the alive abdominal tissue peaks (Figure 1B, arrow). Compiling data from multiple animals revealed that the resonant frequency values of murine abdominal tissues significantly decreased after the animals were euthanized ($9.48 \times 10^7 \pm 1.85 \times 10^6$ Hz vs $7.6 \times 10^7 \pm 2.55 \times 10^6$ Hz, live vs dead, n = 16, $^{‡‡}p \leq 1 \times 10^{-7}$) (Figure 1C), serving as a surrogate for a dead or non-viable tissue.

Since we noted significant differences in resonant frequency values with the abdominal scans, the experiment was repeated focusing on the mouse flank to determine if tissues in other areas of the body would yield similar results. Scans were obtained using the same methods as for the abdominal tissue, with the only difference being the location of placement of the resonant sensor on the animal, e.g., on the flank (Figure 1D). Similar to the scans of the abdomen, there was a left shift on the x axis of the dead mouse flank tissue peaks compared to the alive mouse flank peaks (Figure 1E, arrow) and a statistically significant decrease in resonant frequency values (measured at trough, dagger symbol (†)) of the mouse flank following euthanasia ($1.02 \times 10^8 \pm 3.41 \times 10^6$ Hz vs $9.18 \times 10^7 \pm 3.56 \times 10^6$ Hz, live vs dead, n = 8, $^{*}p \leq 0.05$) (Figure 1F). The resonant sensor data obtained for both the abdominal and flank tissues of the murine models demonstrated the ability of the LC sensor to distinguish between live and dead tissues in proximal regions.

https://doi.org/10.1021/acsomega.2c04345
ACS Omega 2022, 7, 32690−32700

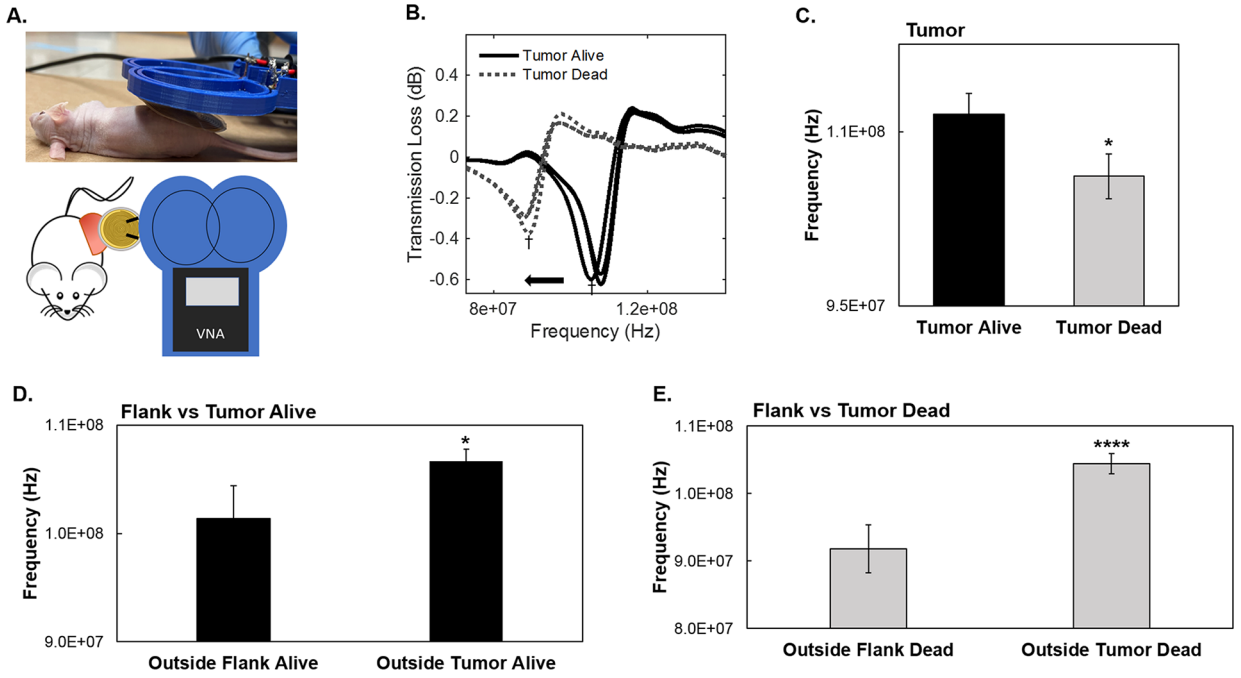

Figure 2. Scanning *in vivo* tumors using the LC sensor. (A) An LC sensor was used to determine the resonant frequency of osteosarcoma, neuroblastoma, medulloblastoma, and neuroendocrine tumors located in the flanks of athymic nude mice. At a tumor volume of 2000 mm^3, the LC sensor was placed onto the flank tumor and the VNA was positioned 1 cm above the sensor. Scans were obtained prior to (alive) and 5 min following (dead) euthanasia. (B) Representative scan from a single animal bearing an osteosarcoma tumor. There was a significant decrease in the resonant frequency (measured at trough, dagger symbol) between viable and non-viable flank osteosarcoma tumor tissues ($n = 9$) seen by a left shift (arrow) on the x axis. (C) There was a statistically significant decrease in resonant frequency values of the flank tumors following euthanasia. (D) Resonant frequencies were compared between flank with no tumor and flanks bearing osteosarcoma tumors. Resonant frequency of flanks with ($n = 18$) tumors was significantly increased when compared to flanks without tumors ($n = 9$). (E) Resonant frequencies of flanks with ($n = 18$) and without ($n = 9$) tumors following euthanasia (dead) were measured. Findings were similar to the alive data, with tumor bearing flanks having a significantly greater resonant frequency than those without a tumor as denoted. A minimum of three scans were obtained for each data point. Photo taken by the authors. Data reported as mean ± SEM. Student's t-test was used to determine statistical significance. $^*p \leq 0.05$, $^{****}p \leq 0.0001$.

Scanning *In Vivo* Tumors Using the LC Sensor. Once the resonant sensor system could detect differences in resonant frequency between alive and dead benign tissues, studies were advanced to evaluate tumor tissues. The resonant frequency of established solid tumors (osteosarcoma, neuroblastoma, medulloblastoma, and neuroendocrine) located in the flanks of athymic nude mice was measured. At a tumor volume of 2000 mm^3, a minimum of three scans were obtained prior to euthanasia using the scheme as previously described (Figure 2A). Five minutes post-euthanasia, the resonant frequency of the tumor tissue was measured with a minimum of three scans for each animal. Figure 2B depicts a representative output of the data obtained from the MetroVNA for one of the animals in this data set with an established osteosarcoma. As shown in the experiments with non-tumor tissues, there was a significant difference in the resonant frequency between alive (pre-euthanasia) and dead (post-euthanasia) flank tumor tissues with a shift of the x axis to the left ($1.06 \times 10^8 \pm 1.18 \times 10^6$ Hz vs $1.02 \times 10^8 \pm 1.28 \times 10^6$ Hz, live vs dead, $^*p \leq 0.05$, $n = 9$) (Figure 2C).

Next, the resonant frequencies of the flanks without a tumor were compared to those with a tumor. First, a viable murine flank tissue was compared to the viable flank tumor tissue. There was a significant difference between the two groups, with the live flank tumor tissue having a larger resonant frequency value than the flanks without tumors ($1.01 \times 10^8 \pm 3.03 \times 10^6$ Hz vs $1.07 \times 10^8 \pm 1.08 \times 10^6$ Hz, live flank with a tumor ($n = 18$) vs live flank without a tumor ($n = 9$), $^*p \leq 0.05$) (Figure 2D). In the second experiment, flank tumors were scanned over time and demonstrated a significant change in resonant frequency as the tumors increased in size (Figure S1). Next, the dead (post-euthanasia) flank tissue was compared to the dead flank tumor tissue. Again, there was a significant difference between the two groups, with the dead flank tumor tissue having a larger resonant frequency value ($9.18 \times 10^7 \pm 3.56 \times 10^6$ Hz vs $1.04 \times 10^8 \pm 1.51 \times 10^6$ Hz, dead flank with a tumor ($n = 18$) vs dead flank without a tumor ($n = 9$), $^{****}p \leq 0.0001$) (Figure 2E). These results validate the ability of the LC sensor to consistently detect changes in viability of tissue regardless of the tissue of origin and detect differences between tumor and non-tumor tissues.

Detection of Tumor Type Using the LC Sensor. Different tumor types may show a wide variation in characteristics such as size, necrosis, stromal content, calcifications, and vasculature. As an example, histologic sections of neuroblastoma and osteosarcoma (Figure S2) show a vast difference in morphology. Thus, we suspected that these variations would affect the relative permittivity of the tissue and thus the resonant frequency of the coupled LC sensor leading to the ability to distinguish between tumor types. To test this hypothesis, scans of viable flank tumor tissues from neuroblastoma ($n = 4$), hepatoblastoma ($n = 3$), medulloblastoma ($n= 3$), osteosarcoma ($n = 3$), and neuroendocrine ($n = 2$) tumors were obtained by scanning the tumor-bearing flank, as shown in Figure 2A. Notably, tumors of the same classification clustered around a similar

https://doi.org/10.1021/acsomega.2c04345
ACS Omega 2022, 7, 32690−32700

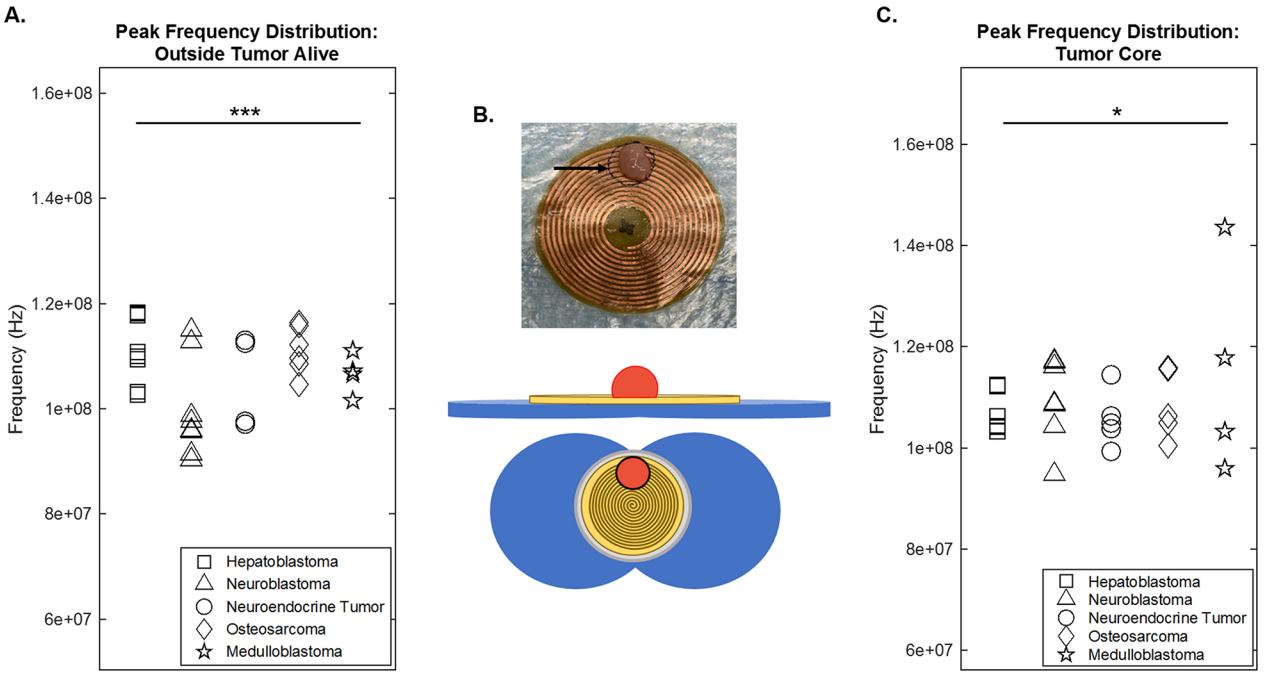

Figure 3. Detection of tumor type using the LC sensor. (A) Scans of flank tumor tissues (*in vivo*) from neuroblastoma (n = 4), hepatoblastoma (n = 3), medulloblastoma (n = 3), osteosarcoma (n = 4), and neuroendocrine tumors (n = 2) were obtained, as shown in Figure 2A. An analysis of variance (ANOVA) demonstrated a significant difference between the peak frequencies of each of the tumor types between each other. (B) A trephine was used to obtain a standard size core (2 mm) of tissues from hepatoblastoma (n = 3), neuroblastoma (n = 5), medulloblastoma (n = 3), osteosarcoma (n = 4), and neuroendocrine (n = 4) flank tumors. The tissue cores were placed on the LC sensor in the exact same location (black mark indicated by a black arrow in the upper panel) and readings obtained. (C) There was a significant difference in the peak frequency between *ex vivo* tumor types when measuring the tumor cores (ANOVA). A minimum of three scans were obtained for each data point. Photo obtained by the authors. Data presented as mean ± SEM. *$p \leq 0.05$, ***$p \leq 0.001$.

resonant frequency value. An analysis of variance (ANOVA) comparison revealed a significant difference between the peak frequencies of each of the tumor types (***$p \leq 0.001$) (Figure 3A).

There are several effects that may confound readings of the resonant sensor including temperature, sample pressure (mass), and the location of the specimen on the sensor. The next set of experiments was designed to mitigate some of these confounders. Following animal euthanasia and tumor harvest, a standard size core of each tumor was obtained using a 2 mm trephine, as outlined in the Methods section. Tumor core tissues from hepatoblastoma (n = 3), neuroblastoma (n = 5), medulloblastoma (n = 3), osteosarcoma (n = 3), and neuroendocrine (n = 4) tumors were each placed on the LC sensor in the exact same location, as diagramed in Figure 3B (upper panel), and a minimum of three scans were obtained for each tumor core. There was a significant difference in the peak frequency between tumor types (*$p \leq 0.05$) (Figure 3C). Collectively, these results indicate that the resonant frequencies between the tumor types were significant enough to be detected by an LC sensor both *in vivo* and *ex vivo* and that resonant frequencies clustered based upon tumor histology.

Tissue Differentiation Using the LC Sensor. Due to the differences captured in the resonant frequency values of the tumor tissue by the LC sensor, it was logical to next examine whether the LC sensor could detect the resonant frequency of normal murine organs and tissues. Following euthanasia, a trephine was used to harvest a standard 2 mm core of the brain, heart, kidney, liver, lung, pancreas, spleen, and bone. The tissue was scanned using the same schema described in Figure 3B. For each animal (n = 4), a minimum of three *ex vivo* scans of each organ core were obtained. Figure 4A displays the average resonant frequency values obtained for each organ core, and the shifts along the x axis demonstrate the differing resonant frequency values between the organ tissues (Figure 4A). A statistical analysis of the organ and bone data demonstrated that each tissue type had significantly different average resonant frequency values (Figure 4B). These results demonstrate the potential of the LC sensor to distinguish between different tissue types. The results obtained corroborate previous LC sensor studies performed on biological tissues, which demonstrated the differences in dielectric properties of tissues.[11,12]

The resonant frequencies of excised tumors to their tissues of origin were then compared. Looking at the medulloblastoma tumor tissue compared to a healthy brain tissue (n = 3) revealed a significantly higher resonant frequency value in the tumor tissue ($9.31 \times 10^7 \pm 4.28 \times 10^5$ Hz vs $1.10 \times 10^8 \pm 1.78 \times 10^6$ Hz, medulloblastoma vs brain, $^{\ddagger\ddagger}p \leq 1 \times 10^{-7}$) (Figure 4C). The second set of scans compared the excised hepatoblastoma tumor to the healthy liver tissue (n = 3), and again, the tumor demonstrated a significantly higher resonant frequency ($9.38 \times 10^7 \pm 9.22 \times 10^5$ Hz vs $1.01 \times 10^8 \pm 2.56 \times 10^6$ Hz, hepatoblastoma vs liver, **$p \leq 0.01$) (Figure 4D). The final set of scans compared osteosarcoma to the bone, but unlike the previous tissues, the tumor had a significantly lower resonant frequency value (n = 3) ($1.26 \times 10^7 \pm 9.34 \times 10^4$ Hz vs $1.10 \times 10^8 \pm 1.69 \times 10^6$ Hz, osteosarcoma vs bone, $^{\ddagger\ddagger}p \leq 1 \times 10^{-7}$) (Figure 4E). These comparative scans collectively displayed that the tumor tissue

https://doi.org/10.1021/acsomega.2c04345
ACS Omega 2022, 7, 32690−32700

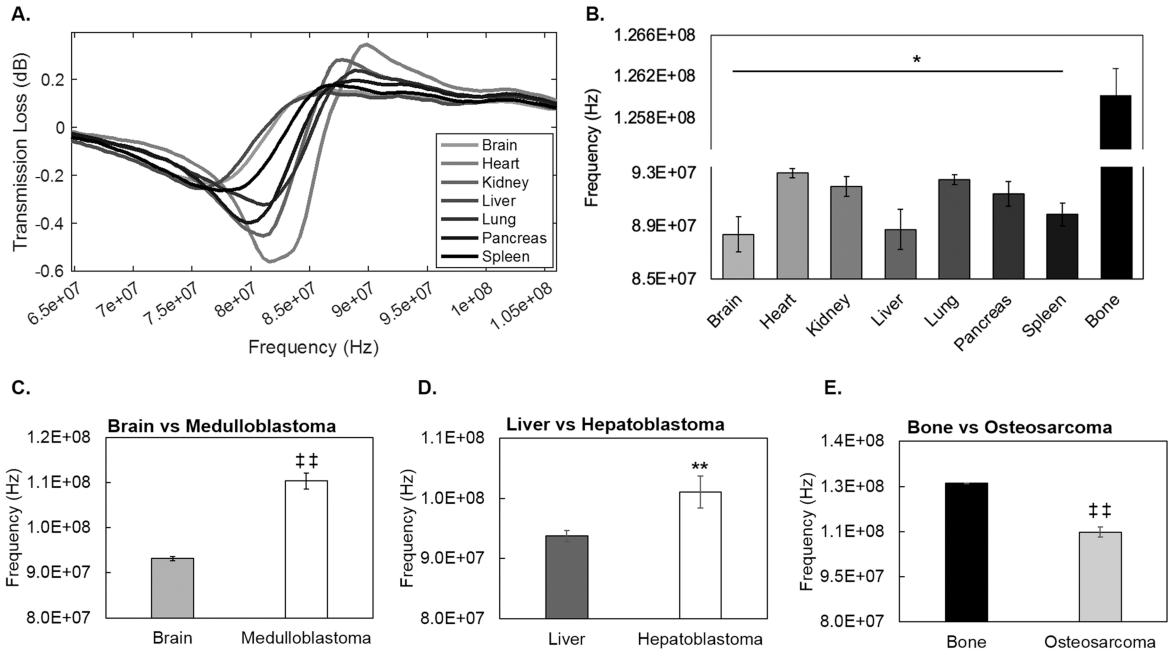

Figure 4. Tissue differentiation using the LC sensor. (A) A standard 2 mm core of the brain, heart, kidney, liver, lung, pancreas, spleen, and bone was scanned, as described in Figure 3B. For each mouse (n = 4), we obtained a minimum of three *ex vivo* scans of each organ core. The graph displays the average resonant frequency values obtained for each organ core, and the shifts along the x axis demonstrate the differing resonant frequency values between the organ tissues. (B) Compiled data (n = 4 animals). Each tissue type had significantly different average resonant frequency values (ANOVA). (C–E) The resonant frequencies of tumors (2 mm cores) were compared to their tissues (2 mm cores) of origin. (C) Medulloblastoma (n = 3) had a significantly higher resonant frequency than the brain (n = 4). (D) Hepatoblastoma (n = 3) had a significantly greater resonant frequency than a normal liver (n = 4). (E) Osteosarcoma (n = 4) had a significantly lower resonant frequency than a normal bone (n = 4). A minimum of three scans were obtained for each data point. Data reported as mean ± SEM. For statistical comparisons, analysis of variance (ANOVA) was used for the tissue cores and Student's t-test for tissue vs tumor types. $^{*}p \leq 0.05$, $^{**}p \leq 0.01$, $^{‡‡}p \leq 1 \times 10^{-7}$.

has a different resonant frequency than its non-pathologic tissue of origin, and the LC sensor detects such differences.

LC Sensor Detects Differences in Resonant Frequency between Primary and Metastatic Tumors. Tumor metastasis often demonstrates different physical properties than the primary tumors. We hypothesized that an LC sensor would demonstrate differences in resonant frequencies between tissues from metastases compared to the primary tumor tissue. We also hypothesized that an LC sensor would show that the metastatic site may have a different resonant frequency than the same site without malignant tissues. Using a PDX model of a metastatic human neuroendocrine tumor, both *in vivo* and *ex vivo* tissue scans were completed for mice that harbored intraperitoneal abdominal metastases. The method for obtaining the *in vivo* resonant sensor data followed the same procedure shown in Figure 1A, with at least three scans obtained for each animal. The resonant frequency values of abdomens with metastatic neuroendocrine tumors were compared to the values from neuroendocrine tumors in the flank of live mice. The scans of *in vivo* abdominal metastasis demonstrated a decrease in resonant frequency as compared to the scans of the *in vivo* flank tumors, indicated by a left shift on the x axis (Figure 5A, arrow). The metastatic tumors (n = 6) had a significantly lower resonant frequency value than that of the flank tumor (n = 5) ($7.31 \times 10^7 \pm 1.05 \times 10^6$ Hz vs $1.05 \times 10^8 \pm 3.41 \times 10^6$ Hz, metastasis vs flank tumor, $^{‡}p \leq 1 \times 10^{-6}$) (Figure 5B). Next, tumor cores from abdominal metastatic and flank neuroendocrine tumors were scanned as described (Figure 3B). As with the *in vivo* scans, the *ex vivo* data (tissue cores) demonstrated a significant difference in frequency between the two specimen types (Figure 5C), with the metastatic tumor having a lower resonant frequency value ($1.07 \times 10^8 \pm 6.92 \times 10^5$ Hz vs $1.03 \times 10^8 \pm 8.11 \times 10^5$ Hz, metastasis vs flank tumor, $^{***}p \leq 0.001$) (Figure 5D). These data demonstrate a difference between metastatic and primary tumor tissue resonant frequency and that the resonant sensor detected these differences both *in vivo* and *ex vivo*.

Since the location of the metastasis may affect resonant frequency, animals without peritoneal metastasis were compared to those with metastatic disease. The abdomen scans from animals bearing metastases displayed a higher resonant frequency than the scans of abdomens in animals without metastases as demonstrated by a right shift on the x axis (Figure 5E, arrow). Statistical analysis confirmed a significantly higher resonant frequency in abdomens of animals with metastatic tumors ($7.31 \times 10^7 \pm 1.05 \times 10^6$ Hz vs $6.63 \times 10^7 \pm 8.11 \times 10^5$ Hz, metastasis vs no metastasis, $^{*}p \leq 0.05$) (Figure 5F). These data highlight the capacity of the LC sensor to detect the presence of tumor metastasis *in vivo*.

Chemotherapy Alters Resonant Frequency. Last, we investigated whether the LC sensor could detect changes in tumor tissues following treatment. Animals bearing flank tumors of SK-N-AS human neuroblastoma cells were treated with a protein phosphatase 2A (PP2A) activator (ATUX-792). In brief, once tumor volumes reached 100 mm^3, animals were randomized to receive either vehicle (n = 5) or ATUX-792 (n = 7, 50 mg kg^{-1} via gavage twice per day). At completion of therapy, the flank tumors were scanned, and scans were compared between treated and untreated tumors. The left shift on the x axis represents the decrease in resonant frequency (measured at trough, dagger symbol (†)) of the ATUX-792

https://doi.org/10.1021/acsomega.2c04345
ACS Omega 2022, 7, 32690−32700

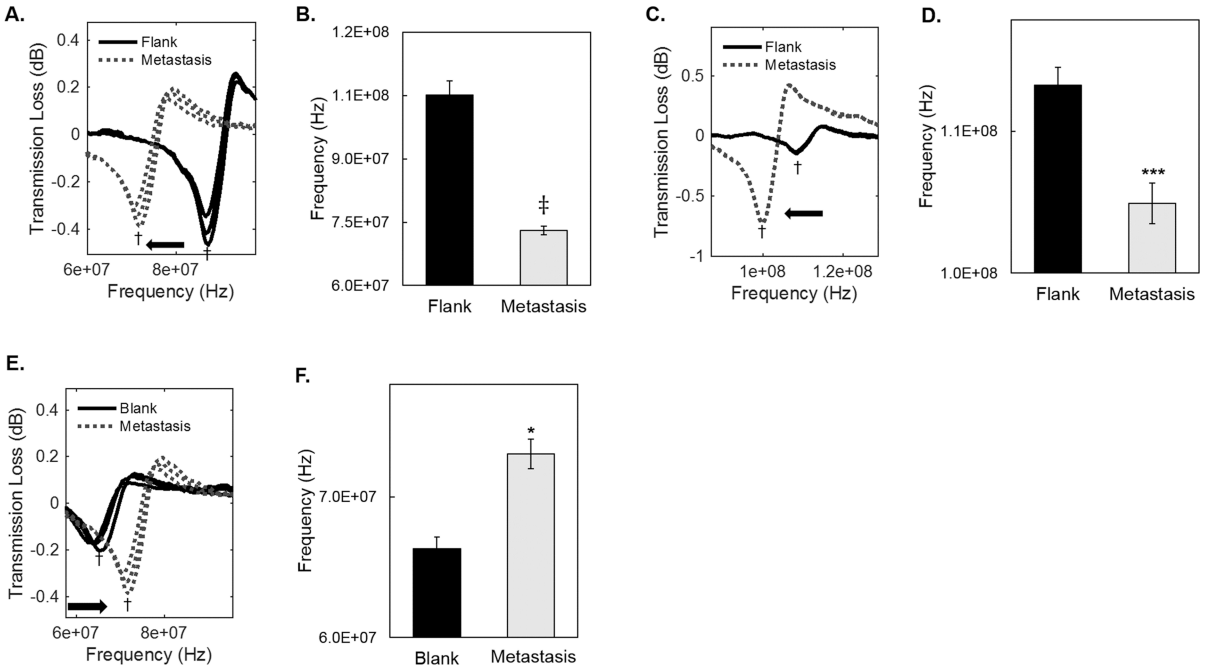

Figure 5. LC sensor detects differences in resonant frequency between primary and metastatic tumors. (A) LC sensor was used to obtain resonant frequency scans using a PDX model of a metastatic human neuroendocrine tumor. Scans were compared between tumors grown in the flank (primary) and those grown as intraperitoneal metastases. Representative scans from a single animal demonstrate a shift to the left of the *x* axis (arrow) of resonant frequency (measured at trough, dagger symbol) from the flank tumor compared to the abdominal metastatic tumor. (B) The metastatic tumors ($n = 6$) had a significantly lower resonant frequency value than that of the flank tumors ($n = 5$). (C) Tumor tissue cores from abdominal metastatic and flank neuroendocrine tumors were scanned (Figure 3B). A representative scan demonstrates the left shift in the *x* axis (arrow) of resonant frequency (measured at trough, dagger symbol) between the flank tumor cores and the cores from abdominal metastases. (D) The metastatic tissue cores demonstrated significantly lower frequency than the flank tumor cores. (E) Scans of the abdomen were compared between animals without abdominal metastases (blank) and those with abdominal metastases. A representative scan shows the right shift of the *x* axis (arrow) between resonant frequency (measured at trough, dagger symbol) of the blank abdomen (no tumor) and the abdomen bearing tumor metastases. (F) The abdomen scans from animals bearing metastases displayed a higher resonant frequency than the scans of abdomens from animals without the metastatic tumor. Data reported as mean ± SEM. Student's *t*-test was employed for statistical comparisons. $^{*}p \leq 0.05$, $^{***}p \leq 0.001$, $^{\ddagger}p \leq 1 \times 10^{-6}$.

treated tumors compared to the untreated tumors (Figure 6A, arrow). Statistical analysis confirmed that the treated tumors had a significantly lower resonant frequency than the untreated tumors ($1.20 \times 10^8 \pm 9.51 \times 10^5$ Hz vs $1.12 \times 10^8 \pm 3.10 \times 10^6$ Hz, untreated vs treated, $^{**}p \leq 0.01$) (Figure 6B). Finally, scans of treated and untreated tumor cores were compared. Findings were consistent with those of the flank scans, demonstrating a left shift on the *x* axis for resonant frequency (Figure 6C, arrow). The ATUX-792 treated tumor cores had a significantly lower resonant frequency value than the cores of untreated tumors ($1.21 \times 10^8 \pm 3.81 \times 10^6$ Hz vs $1.11 \times 10^8 \pm 1.86 \times 10^6$ Hz, treated core vs untreated core, $^{**}p \leq 0.01$) (Figure 6D). Since these trends followed those between viable and non-viable tissues (Figure 1), the ATUX-792 treated tumors were evaluated further. Untreated tumors showed a significant increase in tumor necrosis (Figure S3). These data demonstrate that the resonant sensor has the ability to detect changes in resonant frequencies between treated and untreated tumors and viable and necrotic tumor tissues.

DISCUSSION

In the current study, we investigated whether tissue permittivity changes would allow detection between live and non-viable tissues. This determination has potential to guide a wide range of clinical decisions regarding tumor specimen viability and adequacy, the presence of organ ischemia, or progression of wounds.

Data from the current study show that resonant frequency values of live compared to non-viable tissues are significantly different. A left shift in frequency was observed in non-viable tissues compared to live tissues irrespective of location (abdomen or flank) or type of tissue (tumor versus normal tissue). Readings for the non-viable tissues were made following animal euthanasia. A potential explanation for the study findings may be changes in temperature. Temperature has been demonstrated to affect tissue permittivity such that the dielectric properties of *ex vivo* bovine and porcine tissue changed about 1% per °C of tissue cooling.[13] Since measurements in the current studies were performed after only 5 min following animal euthanasia, it is unlikely that the significant changes detected by the LC sensor could be contributed entirely to changes in temperature.

The ability to detect normal tissues from tumor tissues using changes in tissue permittivity has clinical relevance in the recognition of complete tumor resection margins, detecting tumor metastasis without invasive techniques, and even assisting in rapid tissue diagnostics. In the current study, the resonant sensor detected a significant difference in tissue permittivities between different types of tumors, between normal tissues and their associated tumors, and even in the presence of metastasis. Our findings corroborate findings from other researchers. O'Rourke and colleagues demonstrated that

https://doi.org/10.1021/acsomega.2c04345
ACS Omega 2022, 7, 32690−32700

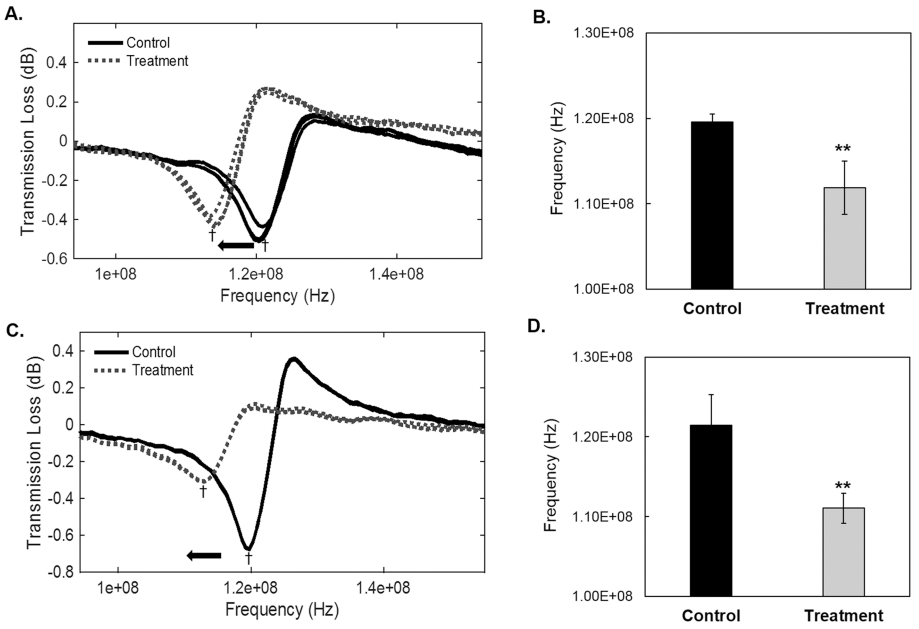

Figure 6. Chemotherapy alters resonant frequency. (A) Animals bearing SK-N-AS neuroblastoma flank tumors were treated with a small-molecule protein phosphatase 2A (PP2A) activator (ATUX-792). Once tumor volumes reached 100 mm^3, animals were randomized to receive either vehicle (n = 5) or ATUX-792 (n = 7) via oral gavage. Prior to animal euthanasia, the flank tumors were scanned. Representative scan of a treated (ATUX-792) and control (vehicle) tumor demonstrated a left shift in the x axis (arrow) of the resonant frequency (measured at trough, dagger symbol) of the treated tumor. (B) Statistical analysis confirmed that the treated tumors had a significantly lower resonant frequency than the untreated tumors. (C) Scans were performed on tumor cores and compared between treated (ATUX-792) and untreated (vehicle) tumors. A representative scan of a core of the treated and core of the control tumor demonstrated a left shift in the x axis (arrow) in the resonant frequency (measured at trough, dagger symbol) of the treated tumor. (D) Tissue cores from ATUX-792 treated tumors had a significantly lower resonant frequency value than the cores of untreated tumors. A minimum of three scans were obtained for each data point. Data are reported as mean ± SEM. Statistical comparisons were completed with Student's t-test. $^{**}p \leq 0.01$.

the dielectric properties of hepatocellular carcinoma, an adult primary liver tumor, and other metastatic tumors in the liver were 16% higher than normal liver tissues.[10] We noted similar findings in our study where the resonant frequency of the hepatoblastoma tissue, a pediatric liver cancer, was 7% higher than normal liver tissues.

There are many potential explanations for the differences in tissue permittivity of tumor tissue compared to normal tissues and variance between tumor types. The water versus lipid content of tissues and tumors is well documented and serves as a basis for imaging techniques such as computerized tomography, magnetic resonance imaging, and diffuse optical spectroscopy.[14] These differences in water content affect the tissue permittivity, with the relative permittivity of water being about 80 times that of lipids.[15] These differences in water content would allow the resonant sensor to distinguish between different types of tumors and also between tumor and normal tissues. The water content of the tissues may also be affected by cell processes such as apoptosis and necrosis. These changes in tissue water content would be one explanation for the noted changes in tissue permittivity demonstrated in tumors that were treated with chemotherapeutics since they demonstrated significant necrosis after treatment.

The water content of tissues is also affected by blood flow, which varies significantly between organ systems. For example, the liver receives about 27% of the cardiac output compared to about 21% in the skeletal muscle. For the current study, to mitigate this potential confounder, tumor tissues and organs were scanned *ex vivo* soon after animal euthanasia before significant fluid losses through dehydration occurred. Therefore, the differences noted between resonant frequencies of different organs or between flank and abdomen alive versus dead tissues were likely not entirely secondary to blood flow. Additionally, electrical conductivity of human tissues varies depending upon pH and ionic makeup of the tissues. Studies evaluating resonant frequencies of ionic solutions demonstrated differing resonant frequencies that could be predicted based upon the ionic content.[16] Based on these findings, we postulate that the differences in resonant frequencies in the organs and tissues studied might be attributed to variances in their ionic makeup, rather than blood flow.

The current resonant sensor design is based on a passive sensor platform.[3] The advantages to using this LC sensor system for characterizing biologic tissues are several. The design is inexpensive to fabricate, which improves accessibility to research groups and to health care professionals who practice in resource limited areas, broadening the spectrum of potential applications of the system. It also lends itself well for single-use applications, such as integration into surgical pads, for convenient use during surgery to rapidly assess tissue quality. Further, the VNA employed in the current design has Bluetooth capabilities and does not require a direct power source, rendering the LC sensor versatile in widely differing environments.

Aside from the physical and financial advantages of the resonant sensor system presented in these studies, the data that the system is capable of generating are valuable and have the potential for multiple clinical applications. For example, based on the capability of the resonant sensor system to detect differences between normal versus tumor tissues and between alive (viable) and dead (non-viable) tissues, we believe that the

https://doi.org/10.1021/acsomega.2c04345
ACS Omega 2022, 7, 32690−32700

resonant sensor system would allow for rapid detection of core needle sample adequacy, potentially abrogating the need for a more invasive procedure for solid tumor biopsy. Further, the ability to differentiate a normal from a tumor tissue could aid in the real-time determination of tumor resection margins. Finally, the ability to detect metastatic disease could lead to the elimination of invasive lymph node sampling that is currently required for many tumor diagnoses such as breast cancer and melanoma.

As with any experimental device, there are drawbacks to using LC sensors to measure the biologic activity of a system. The resonant frequency of the resonant sensor and reader system is dependent upon the mutual inductance between the sensor and reader. Mutual inductance is a function of a coupling constant, which depends upon positional alignment between the two inductors: the sensor and the reader.[17] If the tissues are scanned in positions that are significantly different from one another, then the corresponding resonant frequency values obtained will not accurately represent the tissue permittivity.[18] The experiments in this study were designed to control for the sensor position. When resonant frequency values were obtained for the live murine models, the exact position of the resonant sensor and reader was kept constant between the experimental groups. When the tissues were excised and scanned by being placed on top of the resonant sensor system, the tissues were always placed in the exact same location on the sensor, and the sensor itself was also placed in a constant location on the reader. The LC sensor is also subject to pressure variations that deform the resonant sensor leading to changes in inductance and capacitance.[19,20] If the pressure applied to the sensor by the experimental tissue is not constant, then the data obtained may not accurately represent the tissue permittivity and may not be reproducible. The current experimental design factored in the variable of pressure. When the resonant frequency was obtained for the live murine models, the distance between the reader and the sensor was kept constant to ensure that a constant pressure was applied between the two experimental devices across the study. For the *ex vivo* studies, a sterile 2 mm trephine was used to sample every tissue examined. Excising all the tissues to the same volume significantly reduced the amount of pressure variation between the tissues. Recent studies have been performed to overcome the positional alignment sensitivity issues of the LC sensor.[21,22] By understanding the potential implications of misaligning the resonant sensor system and maintaining consistent pressure on the system for the various experiments, we were able to successfully design the experiments to control for potential frequency variation and confidently report the data.

CONCLUSIONS

The findings of this study demonstrate that a portable, wireless, LC resonant sensor system was capable of accurately characterizing pediatric solid tumors both *in vivo* and *ex vivo*. By detecting the permittivity of the tissue, the LC sensor differentiated between live and dead tissues and between an array of murine organs including the brain, spleen, liver, pancreas, lung, kidney, and heart. The ability to differentiate these tissues led to characterization between (i) pediatric solid tumors of differing histology, (ii) normal tissues and tumor tissues, (iii) primary and metastatic tissues, and (iv) treated and untreated tumors. Based on these findings, we postulate that the LC sensor system could be translated for novel clinical cancer applications that may vastly improve the quality of care for patients. For example, the resonant sensor technology could assist in the rapid determination of adequacy of tumor biopsy specimens from the standpoint of obtaining a viable tissue for diagnosis. The ability to accurately differentiate between cancerous and healthy tissue demonstrates the potential role of the LC sensor in the rapid determination of adequacy of tumor resection margins. Other clinical applications include the early detection of metastasis, based on changes in tissue permittivity. We will continue exploring the potential for clinical applications of the LC sensor system as we believe that the technology will have a pivotal role in future pediatric cancer research and therapy.

METHODS

Resonator Fabrication. A Silhouette Curio X-Y plotter (Silhouette America, Inc., Lindon, UT) was used in combination with an ultrafine point permanent sharpie marker to mask an Archimedean spiral on the copper surface of copper-coated polyimide (DuPont Pyralux, DuPont, Torrance, CA). The Archimedean spirals were designed using the CAD software Rhinoceros5 (https://www.rhino3d.com) to have a 40 mm outer diameter with a pitch size of 1.2 mm. After the spiral was masked onto the polyimide, the unmasked copper was etched from the surface by submerging it into a 2:1 volume ratio solution of hydrogen peroxide/hydrochloric acid (H_2O_2/HCl). Acetone was then used to remove the mask from the resonator, and the resonator was air-dried and encapsulated in a Tegaderm dressing (3M, Maplewood, MN).

Signal Acquisition. A MetroVNA Deluxe 250 MHz (Metropwr, Italy) acquired the data. This portable vector network analyzer (VNA) was used in combination with a three-dimensionally (3D) printed antenna holder to create the resonant reader. The printed holder contained a dual-loop coil antenna with 54 mm diameter copper loops, with an overlap of 26.7 mm^3.[3] The VNA in conjunction with JAVA-based software, vna/J (https://vnaj.dl2sba.com/), generated the tissue resonant sensor data. The VNA monitored the S21 parameter in the scattering parameter matrix.[23] The scans had a start frequency of 0.1 MHz and an end frequency of 1.8 MHz, and the number of points (or frequency step size) was 10,000 kHz. The basic scan setup is diagrammed in Figure S4.

Data Analysis. The VNA used in the experiments determined the transmission loss of the resonant sensor system. The transmission loss of the resonant sensor system changes in both amplitude and peak frequency based on the permittivity of the medium exposed to the resonant sensor.[8] Once the data were collected for each experiment via the MetroVNA, they were imported into the numeric computing platform MATLAB for analysis (https://www.mathworks.com/products/matlab.html) (Figure S5). Several features of the S21 parameter were quantified for the various experiments including transmission loss and peak frequency of the resonant sensor system.

Resonant Sensor Data Collection. All tissues assessed by the resonant sensors were human in origin propagated in athymic nude mice (Fredricks, Charles River, Wilmington, MA). For external live tissue scans, animals were anesthetized with 3% isoflurane and placed in the supine position, and the LC sensor was placed on the center of the area of interest. The reader was then placed over the center of the LC sensor, and the vna/J software was used to obtain the transmission loss data from the reader. The University of Alabama at

https://doi.org/10.1021/acsomega.2c04345
ACS Omega 2022, 7, 32690−32700

Birmingham Institutional Animal Care and Use Committee (UAB IACUC) approved all animal experiments (IACUC-022020), and experiments were conducted within institutional, national, and NIH guidelines. After resonant frequency readings were recorded, the animals were humanely euthanized per IACUC protocols with CO_2 in their home cages followed by cervical dislocation. Five minutes after euthanasia, the resonant sensor and reader were used in a similar fashion to obtain scans of an external dead tissue. Comparisons were completed between the relative permittivities of a live versus dead tissue and between external tissue types and conditions. External tissue areas scanned included the abdomen, flank, and established flank pediatric solid tumors.

To obtain scans of internal tissues, mice were euthanized as described above. The tissue of interest was extracted from the mouse following euthanasia under sterile conditions outlined by IACUC protocols (IACUC-022020). To minimize water loss from the specimen, immediately following tissue harvest, a 2 mm trephine was used to cut a standard, uniform core of the selected tissue, which was immediately placed on the resonant sensor. The core of the tissue was placed on the furthest edge of the resonant sensor, with the center of the tissue oriented on the outside end of the Archimedean spiral to control for any variation between experimental samples. This attention to positioning was important as the outside of the resonator is more sensitive than the center.[24] The reason for this difference in sensitivity is because the electromagnetic field inner arms of the Archimedean LC resonator have greater destructive interference than the outer arms.[8] Samples were placed on the sensor in the same location for each reading. The resonant sensor was then positioned in the center of the reader, and scans were obtained as previously described. Internal tissues included the brain, heart, kidney, liver, lung, pancreas, spleen, bone, and established pediatric solid tumors. The resonant frequencies were compared across tissue types. All scanning procedures were conducted under similar conditions, and prior to each scan, the MetroVNA was calibrated to reduce the background signal from the resonant sensor. Each specimen was scanned, removed, replaced, and scanned again at least three times to account for variation caused by positioning.

Tumor Models. Flank tumors were established in 6 week old female athymic nude mice (Fredrick, Charles River, Fredrick, MD). The UAB IACUC (IACUC-022020) approved all experiments. Experiments were conducted within institutional, national, and NIH guidelines. Animals were maintained in the specific pathogen-free facility with standard 12 h light/dark cycles and access to chow and water *ad libitum*. Long-term passage human neuroblastoma SK-N-AS cells (1.8×10^6) in 25% Matrigel (BD Biosciences, San Jose, CA) were injected into the right flank of the animals. To propagate patient-derived xenograft tumors, a piece of tumor (100 mm^3) (neuroblastoma, hepatoblastoma, osteosarcoma, medulloblastoma, and neuroendocrine tumors) was injected into the right flank of mice in a 50% Roswell Park Memorial Institute 1640 Medium (RPMI) and 50% Matrigel (BD Biosciences). We developed these PDXs at our institution under IACUC (IACUC-09186) and UAB Institutional Review Board (IRB, IRB-130627006) approval. Tumors were monitored weekly with caliper measurements and calculation of tumor volume accomplished using the formula $\frac{(\text{length} \times \text{width}^2)}{2}$, where width is the shortest measurement. When tumors reached 2000 mm^3, animals were utilized for scanning experiments.

A second experiment was completed to monitor changes in tissue permittivity in tumors over time. Established human neuroblastoma SK-N-AS cells (1.8×10^6) in 25% Matrigel (BD Biosciences, San Jose, CA) were injected into the right flank of the animals ($n = 20$). These animals were followed for 21 days for tumor growth, and scans were completed at the time of volume measurements.

A unique metastatic model was established using the neuroendocrine PDX. A neuroendocrine PDX flank tumor was harvested and dissociated following our previously published protocol,[9] and cells were kept in culture for 24 h at 5% CO_2 and 37 °C. PDX cells (2×10^6) were then resuspended in 100 μL of sterile phosphate buffered saline (PBS) and injected into the abdominal cavity of the animals via a 27-gauge needle. Animals were weighed weekly, and the overall body condition was monitored daily. Abdomens were palpated routinely, and upon detection of tumors, mice were used for external and internal scans as described above. Established tumor cell lines and PDX tumor cells were validated regularly using short tandem repeat analysis (UAB, Genetics Core). Polymerase chain reaction studies confirmed no murine contamination of the human PDXs (UAB, Genetics Core), and the cells were deemed free of mycoplasma.

***In Vivo* Treatment Studies.** Once SK-N-AS neuroblastoma flank tumors reached a volume of 100 mm^3, animals were randomized to three groups to receive 100 μL of either vehicle [*N*,*N*-dimethylacetamide (DMA, 271012, Sigma-Aldrich) and Kolliphor HS 15 (Solutol, 42996, Sigma-Aldrich), $n = 5$] or ATUX-792 (50 mg kg^{-1} in DMA and Solutol, $n = 7$) twice daily by oral gavage. Flank tumors were scanned prior to euthanasia and 5 min after euthanizing the animals. We then resected the tumors and used a trephine core as described, placing each core on the same location on the resonance sensor. The resonant frequency of tumors treated with vehicle was compared to that of tumors treated with ATUX-792.

In the second study, trametinib (Selleckchem, Houston, TX), a small molecule inhibitor of MEK1/2, was tested as a targeted therapeutic against the metastatic neuroendocrine PDX. Metastatic tumors were established as previously described,[9] and drug treatment was initiated 24 h after injection of cells. An external tissue scan of the abdomen was obtained prior to treatment initiation. Mice received 2 mg kg^{-1} trametinib ($n = 5$) or 4% dimethyl sulfoxide (DMSO, vehicle, $n = 5$) in corn oil via oral gavage daily. External abdominal tissue scans were obtained three times a week for a total of 6 weeks. Due to the limited tumor specimen in the treatment group, tissue core scans of the tumors were not obtained. Analysis of the relative permittivities was compared over time and between experimental groups.

Statistical Analysis. All scans were performed in at least triplicate, and data were represented with at least three biologic replicates. Data were reported as mean ± SEM. Statistical analysis was completed with GraphPad Prism 9. Student's *t*-test or analysis of variance (ANOVA) was used as appropriate to determine statistical significance. A p-value ≤ 0.05 was considered significant.

■ ASSOCIATED CONTENT

Supporting Information

The Supporting Information is available free of charge at https://pubs.acs.org/doi/10.1021/acsomega.2c04345.

https://doi.org/10.1021/acsomega.2c04345
ACS Omega 2022, 7, 32690−32700

Data for changes in the resonant sensor of flank tumors over time, neuroblastoma and osteosarcoma histology, examples of histology demonstrating tumor necrosis, examples of the system setup, and MATLAB code for data analysis (PDF)

AUTHOR INFORMATION

Corresponding Authors

Nigel F. Reuel − *Department of Chemical and Biological Engineering, Iowa State University, Ames, Iowa 50111, United States;* orcid.org/0000-0003-3438-2919; Phone: (515) 294-4592; Email: reuel@iastate.edu

Elizabeth A. Beierle − *Division of Pediatric Surgery, Department of Surgery, University of Alabama at Birmingham, Birmingham, Alabama 35233, United States;* orcid.org/0000-0002-4613-0527; Phone: (205) 638-9688; Email: elizabeth.beierle@childrensal.org

Authors

Andee M. Beierle − *Department of Radiation Oncology, University of Alabama at Birmingham, Birmingham, Alabama 35233, United States*

Colin H. Quinn − *Division of Pediatric Surgery, Department of Surgery, University of Alabama at Birmingham, Birmingham, Alabama 35233, United States*

Hooper R. Markert − *Division of Pediatric Surgery, Department of Surgery, University of Alabama at Birmingham, Birmingham, Alabama 35233, United States*

Adam Carr − *Department of Chemical and Biological Engineering, Iowa State University, Ames, Iowa 50111, United States*

Raoud Marayati − *Division of Pediatric Surgery, Department of Surgery, University of Alabama at Birmingham, Birmingham, Alabama 35233, United States*

Laura V. Bownes − *Division of Pediatric Surgery, Department of Surgery, University of Alabama at Birmingham, Birmingham, Alabama 35233, United States*

Sara Claire Hutchins − *Division of Pediatric Hematology/Oncology, Department of Pediatrics, University of Alabama at Birmingham, Birmingham, Alabama 35233, United States*

Jerry E. Stewart − *Division of Pediatric Surgery, Department of Surgery, University of Alabama at Birmingham, Birmingham, Alabama 35233, United States*

Benjamin Hill − *Division of Pathology, Children's Hospital of Alabama, Birmingham, Alabama 35233, United States*

Michael Ohlmeyer − *Atux Iskay LLC., Plainsboro, New Jersey 08536, United States*

Complete contact information is available at: https://pubs.acs.org/10.1021/acsomega.2c04345

Author Contributions

[▽]A.M.B. and C.H.Q. contributed equally to this work. A.M.B. and C.H.Q. conceived the project and developed it together with N.F.R. and E.A.B. and designed and completed all the experiments. A.M.B., A.C., and N.F.R. designed and created the LC sensor. C.H.Q., R.M., L.V.B., S.C.H., and J.E.S. created the murine flank tumors and treated and cared for the animals. B.H. (certified pathologist) completed the histology examinations. M.O. created and synthesized ATUX-792. A.M.B., C.H.Q., and H.R.M. designed and completed MATLAB coding. A.M.B. and C.H.Q. wrote the manuscript. E.A.B. and N.F.R. provided senior guidance, supervised the studies, and edited the manuscript.

Notes

The authors declare the following competing financial interest(s): Michael Ohlmeyer is the inventor of Atux-792 and is the founder of and vice president of chemistry at Atux-Iskay, LLC. The other authors have nothing to declare.

The data that supports the findings of this study are available in the Supporting Information of this article. The other data that support the findings of this study are available from the corresponding author upon reasonable request.

ACKNOWLEDGMENTS

This work was supported in part by a National Science Foundation Industrial Innovation and Partnerships PFI-RP grant under award #1827578 (N.F.R.), National Institutes of Health under the 5T32GM008361 Medical Scientist Training Program (C.H.Q.), and National Cancer Institute of the National Institutes of Health under award number T32 CA229102 (R.M. and L.V.B.). The content is solely the responsibility of the authors and does not necessarily represent the official views of the National Institutes of Health. Other funding sources include Hyundai Hope on Wheels, Kaul Pediatric Research Foundation, Sid Strong Foundation, Elaine Roberts Foundation, and Open Hands Overflowing Hearts (E.A.B.).

REFERENCES

(1) Overman, R. E.; Kartal, T. T.; Cunningham, A. J.; Fialkowski, E. A.; Naik-Mathuria, B. J.; Vasudevan, S. A.; Malek, M. M.; Kalsi, R.; Le, H. D.; Stafford, L. C.; Lautz, T. B. Optimization of Percutaneous Biopsy for Diagnosis and Pretreatment Risk Assessment of Neuroblastoma. *Pediatr. Blood Cancer* **2020**, *67*, No. e28153.

(2) Newman, E. A.; Abdessalam, S.; Aldrink, J. H.; Austin, M.; Heaton, T. E.; Bruny, J.; Ehrlich, P.; Dasgupta, R.; Baertschiger, R. M.; Lautz, T. B.; Rhee, D. S.; Langham, M. R.; Malek, M. M.; Meyers, R. L.; Nathan, J. D.; Weil, B. R.; Polites, S.; Madonna, M. B. Update on Neuroblastoma. *J. Pediatr. Surg.* **2019**, *54*, 383−389.

(3) Charkhabi, S.; Beierle, A. M.; McDaniel, M. D.; Reuel, N. F. Resonant Sensors for Low-Cost. Contact-Free Measurement of Hydrolytic Enzyme Activity in Closed Systems. *ACS Sens.* **2018**, *3*, 1489−1498.

(4) Charkhabi, S.; Jackson, K. J.; Beierle, A. M.; Carr, A. R.; Zellner, E. M.; Reuel, N. F. Monitoring Wound Health through Bandages with Passive LC Resonant Sensors. *ACS Sens.* **2021**, *6*, 111−122.

(5) Benken, A.; Gianchandani, Y. Passive Wireless Pressure Sensing for Gastric Manometry. *Micromachines* **2019**, *10*, 868.

(6) Wang, F.; Zhang, X.; Shokoueinejad, M.; Iskandar, B. J.; Medow, J. E.; Webster, J. G. A Novel Intracranial Pressure Readout Circuit for Passive Wireless LC Sensor. *IEEE Trans. Biomed. Circuits Syst.* **2017**, *11*, 1123−1132.

(7) Dimitrov, K. C.; Song, S.; Chang, H.; Lim, T.; Lee, Y.; Kwak, B. J. Interdigital Capacitor-Based Passive LC Resonant Sensor for Improved Moisture Sensing. *Sensors* **2020**, *20*, 6306.

(8) Carr, A. R.; Patel, Y. H.; Neff, C. R.; Charkhabi, S.; Kallmyer, N. E.; Angus, H. F.; Reuel, N. F. Sweat Monitoring beneath Garments Using Passive, Wireless Resonant Sensors Interfaced with Laser-Ablated Microfluidics. *Npj Digit. Med.* **2020**, *3*, 62.

(9) Quinn, C. H.; Beierle, A. M.; Williams, A. P.; Marayati, R.; Bownes, L. V.; Markert, H. R.; Aye, J. M.; Stewart, J. E.; Mroczek-Musulman, E.; Crossman, D. K.; Yoon, K. J.; Beierle, E. A. Downregulation of PDGFRß Signaling Overcomes Crizotinib Resistance in a TYRO3 and ALK Mutated Neuroendocrine-Like Tumor. *Transl. Oncol.* **2021**, *14*, No. 101099.

(10) O'Rourke, A. P.; Lazebnik, M.; Bertram, J. M.; Converse, M. C.; Hagness, S. C.; Webster, J. G.; Mahvi, D. M. Dielectric Properties

of Human Normal, Malignant and Cirrhotic Liver Tissue: In Vivo and Ex Vivo Measurements from 0.5 to 20 GHz Using a Precision Open-Ended Coaxial Probe. *Phys. Med. Biol.* **2007**, *52*, 4707−4719.
(11) Gabriel, C.; Gabriel, S.; Corthout, E. The Dielectric Properties of Biological Tissues: I. Literature Survey. *Phys. Med. Biol.* **1996**, *41*, 2231−2249.
(12) Gabriel, S.; Lau, R. W.; Gabriel, C. The Dielectric Properties of Biological Tissues: II. Measurements in the Frequency Range 10 Hz to 20 GHz. *Phys. Med. Biol.* **1996**, *41*, 2251−2269.
(13) Jaspard, F.; Nadi, M. Dielectric Properties of Blood: An Investigation of Temperature Dependence. *Physiol. Meas.* **2002**, *23*, 547−554.
(14) Merritt, S.; Gulsen, G.; Chiou, G.; Chu, Y.; Deng, C.; Cerussi, A. E.; Durkin, A. J.; Tromberg, B. J.; Nalcioglu, O. Comparison of Water and Lipid Content Measurements Using Diffuse Optical Spectroscopy and MRI in Emulsion Phantoms. *Technol. Cancer Res. Treat.* **2003**, *2*, 563−569.
(15) Liquids - Dielectric Constants. *Engineering ToolBox*, 2008.
(16) ElSherbiny, O.; Roy, S.; Charkhabi, S.; Carr, A. R.; Beierle, A. M.; Reuel, N. F.; Neihart, N. M. Physically Inspired Circuit Model for Systematic Analysis of Resonant Ion Sensor. In *IEEE International Symposium on Circuits and Systems (ISCAS)*. IEEE: Seville, Spain 2020, *2020*, 1−5, DOI: 10.1109/ISCAS45731.2020.9181221.
(17) J., Finkenzeller, *RFID Handbook: Fundamentals and Applications in Contactless Smart Cards, Radio Frequency Identification and near-Field Communication*, 3rd ed.; Wiley-Blackwell: Oxford, 2010.
(18) Huang, Q. A.; Dong, L.; Wang, L. F. LC Passive Wireless Sensors Toward a Wireless Sensing Platform: Status, Prospects, and Challenges. *J. Microelectromech. Syst.* **2016**, *25*, 822−841.
(19) Charkhabi, S.; Chan, Y. J.; Hwang, D.; Frey, S. T.; Bartlett, M. D.; Reuel, N. F. Kirigami-Enabled, Passive Resonant Sensors for Wireless Deformation Monitoring. *Adv. Mater. Technol.* **2019**, *4*, 1800683.
(20) Fonseca, M. A.; English, J. M.; von Arx, M.; Allen, M. G. Wireless Micromachined Ceramic Pressure Sensor for High-Temperature Applications. *J. Microelectromech. Syst.* **2002**, *11*, 337−343.
(21) Chan, Y. J.; Carr, A. R.; Charkhabi, S.; Furnish, M.; Beierle, A. M.; Reuel, N. F. Wireless Position Sensing and Normalization of Embedded Resonant Sensors Using a Resonator Array. *Sens. Actuators, A* **2020**, *303*, No. 111853.
(22) Chan, Y. J.; Carr, A. R.; Roy, S.; Washburn, C. M.; Neihart, N. M.; Reuel, N. F. Positionally-Independent and Extended Read Range Resonant Sensors Applied to Deep Soil Moisture Monitoring. *Sens. Actuators, A* **2022**, No. 113227.
(23) D.M., Pozar, *Microwave Engineering*, 4th ed.; Wiley: Hoboken, NJ, 2012.
(24) Charkhabi, S.; Chan, Y. J.; Roy, S.; Islam, M. M.; Duffield, B. B.; Jackson, K. J.; Bu, L.; Kim, S. H.; Hillier, A. C.; Neihart, N. M.; Reuel, N. F. Effects of Fabrication Materials and Methods on Flexible Resonant Sensor Signal Quality. *Extreme Mech. Lett.* **2020**, *41*, No. 101027.

https://doi.org/10.1021/acsomega.2c04345
ACS Omega 2022, 7, 32690−32700